

# CLIDD: Cross-Layer Independent Deformable Description for Efficient and Discriminative Local Feature Representation

Haodi Yao · Fenghua He · Ning Hao · Yao Su

**Abstract** Robust local feature representations are essential for spatial intelligence tasks such as robot navigation and augmented reality. Establishing reliable correspondences requires descriptors that provide both high discriminative power and computational efficiency. To address this, we introduce Cross-Layer Independent Deformable Description (CLIDD), a method that achieves superior distinctiveness by sampling directly from independent feature hierarchies. This approach utilizes learnable offsets to capture fine-grained structural details across scales while bypassing the computational burden of unified dense representations. To ensure real-time performance, we implement a hardware-aware kernel fusion strategy that maximizes inference throughput. Furthermore, we develop a scalable framework that integrates lightweight architectures with a training protocol leveraging both metric learning and knowledge distillation. This scheme generates a wide spectrum of model variants optimized for diverse deployment constraints. Extensive evaluations demonstrate that our approach achieves superior matching accuracy and exceptional computational efficiency simultaneously. Specifically, the ultra-compact variant

---

Haodi Yao  
School of Astronautics, Harbin Institute of Technology, China  
E-mail: 20B904013@stu.hit.edu.cn

Fenghua He  
School of Astronautics, Harbin Institute of Technology, China  
E-mail: hefenghua@hit.edu.cn

Ning Hao  
School of Astronautics, Harbin Institute of Technology, China  
E-mail: haoning0082022@163.com

Yao Su  
State Key Laboratory of General Artificial Intelligence, Beijing Institute for General Artificial Intelligence (BIGAI), China  
E-mail: yaosu@g.ucla.edu

matches the precision of SuperPoint while utilizing only 0.004M parameters, achieving a 99.7% reduction in model size. Furthermore, our high-performance configuration outperforms all current state-of-the-art methods, including high-capacity DINOv2-based frameworks, while exceeding 200 FPS on edge devices. These results demonstrate that CLIDD delivers high-precision local feature matching with minimal computational overhead, providing a robust and scalable solution for real-time spatial intelligence tasks.<sup>1</sup>

**Keywords** Keypoint descriptor, feature matching, deformable description.

## 1 Introduction

Advancements in 3D scene reconstruction and spatial intelligence have revolutionized diverse domains ranging from augmented reality (Mildenhall et al., 2021; Kerbl et al., 2023) to autonomous robotics (Katrakalda et al., 2024; Lei et al., 2025). Central to these developments is the capability to accurately recover both camera poses (Agarwal et al., 2010; Sarlin et al., 2019) and spatial geometry from 2D images (Wang et al., 2025, 2024a; Leroy et al., 2024). This capability relies on establishing robust point-wise correspondences across various views, where sparse local feature matching remains the preferred mechanism due to its computational efficiency and structural reliability (Lowe, 2004; Rublee et al., 2011; Dusmanu et al., 2019; Luo et al., 2020; Potje et al., 2024). Specifically, the performance of local feature matching highly depends on the discriminative power of descriptors, which must remain resilient against drastic illumination shifts and large

---

<sup>1</sup> Demo and weights are available at <https://github.com/HITCSC/CLIDD>.

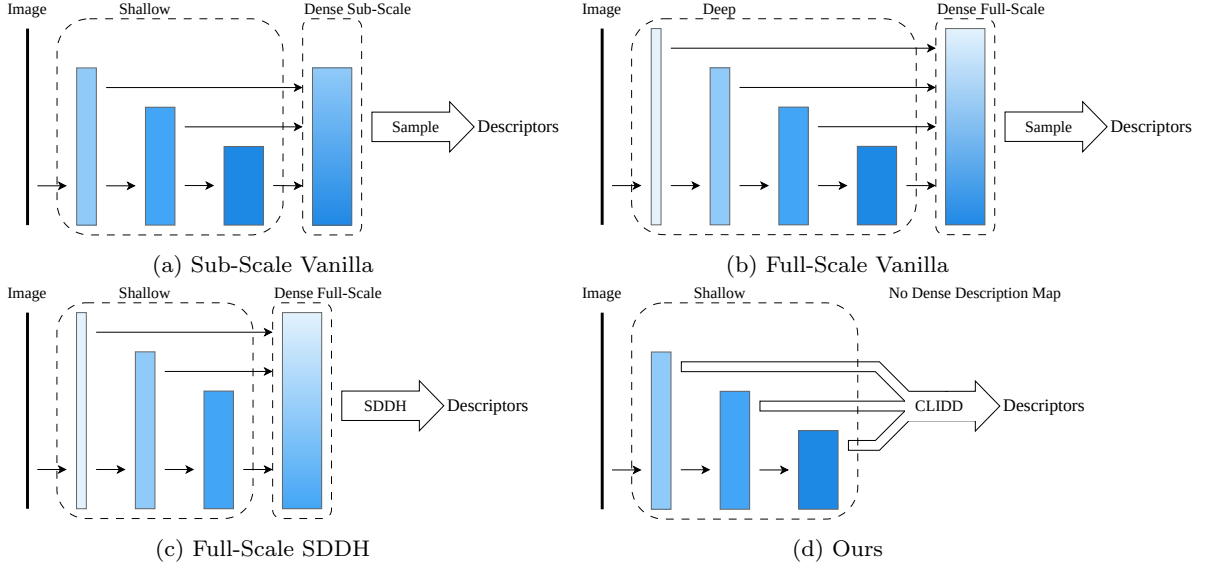


Fig. 1: **Structural comparison of local descriptor extraction strategies.** (a) Sub-Scale Vanilla aggregates multi-scale features into a single low-resolution dense map for sparse sampling. (b) Full-Scale Vanilla constructs a high-resolution, unified feature field to improve precision at the cost of increased memory overhead. (c) Full-Scale SDDH introduces a sparse deformable sampling head on top of the dense, full-scale feature map. (d) Our method employs Cross-Layer Independent Deformable Description (CLIDD) to perform sparse sampling directly from multiple independent feature layers. This strategy generates highly discriminative descriptors while completely bypassing the construction of unified, dense feature maps.

baseline variations (DeTone et al., 2018; Tyszkiewicz et al., 2020).

The quality of local descriptors is primarily determined by how features are aggregated across different network layers. High-performance methods often utilize unified high-resolution feature maps to maximize precision (Tyszkiewicz et al., 2020; Edstedt et al., 2024a). As illustrated in Fig. 1b, these strategies construct a full-scale feature field to preserve fine-grained details during the description process. However, maintaining such dense high-resolution representations requires significant computational resources and a heavy memory burden, which limits their suitability for real-time deployment on resource-constrained devices (Zhao et al., 2023; Gleize et al., 2023).

To improve efficiency, some models bypass intensive upsampling by sampling descriptors directly from low-resolution features (Potje et al., 2024; Yao et al., 2025). This sub-scale approach, illustrated in Fig. 1a, effectively minimizes computational load. However, extracting features from a coarse grid necessitates spatial interpolation to generate descriptors at precise sub-pixel coordinates. When multiple keypoints are located within the same grid cell, they inevitably draw from an identical set of neighboring feature vectors. This results in limited discriminative power of separating nearby fea-

tures, ultimately compromising matching reliability in complex scenarios.

Sparse deformable sampling offers a potential solution by decoupling sampling points from the fixed coordinate grid. By utilizing learnable offsets, each interest point can independently attend to distinct spatial locations and gather unique information from the feature map (Zhao et al., 2023). Nevertheless, the efficiency and flexibility of this approach are often constrained by existing multi-scale integration strategies. Most frameworks, including those utilizing specialized sampling heads, still aggregate all feature levels into a single dense representation before sampling occurs (Fig. 1c). This preliminary fusion step incurs substantial overhead and prevents the sampling process from selectively extracting the most relevant information directly from independent feature layers.

In this work, we present Cross-Layer Independent Deformable Description (CLIDD), a method that generates discriminative descriptors directly from multi-scale hierarchies to avoid the high cost of unified feature maps. This approach utilizes a Cross-Layer Predictor to calculate precise sampling offsets and a Layer-Independent Sampler to extract fine-grained structural details across the feature hierarchy. To optimize execution, we implement a kernel fusion strategy that integrates sampling and aggregation, eliminating com-

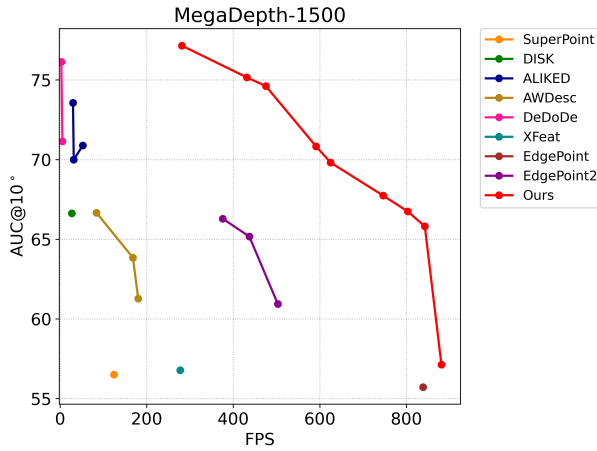


Fig. 2: **Precision-efficiency comparison on resource-constrained devices.** This plot illustrates the relationship between pose estimation accuracy (AUC@10°) on the MegaDepth-1500 benchmark and inference speed (FPS) measured on an edge platform. Our CLIDD-based models consistently occupy the upper-right quadrant, outperforming existing state-of-the-art methods by delivering higher matching precision and significantly faster processing speeds across all configurations.

putational bottlenecks to ensure high-throughput inference across platforms. We integrate CLIDD into a scalable framework that couples lightweight architectures with a training protocol combining metric learning and knowledge distillation. Specifically, we employ DualSoftmax loss for robust description alongside UnfoldSoftmax loss for lightweight detection. We further employ Orthogonal-Procrustes loss for the most compact variants, ensuring high precision despite a minimal parameter count.

The performance of CLIDD is validated through comprehensive experiments across benchmarks for homography estimation, relative pose estimation, and large-scale visual localization. As illustrated in Fig. 2, our models consistently exceed the performance of existing solutions by delivering superior precision and exceptional processing speeds simultaneously. Specifically, our ultra-compact variant matches the precision of SuperPoint (DeTone et al., 2018) with only 0.004M parameters, achieving a 99.7% reduction in model size. Furthermore, the high-performance configuration outperforms state-of-the-art methods, including high-capacity DINOv2-based frameworks (Edstedt et al., 2024a), while exceeding 200 FPS on resource-limited edge devices. Extensive ablation studies and high-density sampling evaluations confirm that our de-

sign achieves simultaneous gains in both accuracy and computational efficiency.

The main contributions are summarized as follows:

- We propose Cross-Layer Independent Deformable Description, utilizing cross-layer offset prediction and independent sampling to capture structural details while bypassing unified feature map overhead. To ensure real-time performance, we implement a kernel fusion strategy that minimizes memory footprint and maximizes inference throughput.
- We introduce a scalable framework that integrates lightweight architectures with a composite training protocol of metric learning and knowledge distillation, yielding diverse model variants optimized for various hardware constraints.
- Extensive evaluations across multiple benchmarks demonstrate that our strategy achieves superior matching precision and efficiency. The proposed descriptors consistently outperform existing high-capacity models in both accuracy and speed, even under challenging high-density sampling conditions.

## 2 Related Work

### 2.1 Keypoint Description

The evolution of local descriptors has been largely shaped by the trade-offs between spatial resolution and computational demand. Early learning-based frameworks (DeTone et al., 2018; Dusmanu et al., 2019; Tang et al., 2019) established the standard of extracting descriptors via interpolation on low-resolution feature maps. Efficiency-oriented models (Potje et al., 2024; Yao et al., 2025) have since optimized this strategy to bypass high-resolution processing bottlenecks. However, relying on a coarse grid often restricts the ability to distinguish fine-grained image structures, as the under-sampled feature volumes provide limited information for generating highly unique representations.

To maximize matching precision, high-performance methods like (Tyszkiewicz et al., 2020; Zhao et al., 2022) utilize dense, high-resolution feature maps. While this approach improves results, it introduces significant memory and processing overhead. Recent advancements such as AWDesc (Wang et al., 2023) integrate Transformer-based components to strengthen representation quality. Specialized architectures like DeDoDe (Edstedt et al., 2024a) further separate detection and description, with the DeDoDe-G variant scaling this architecture using the DINOv2 (Oquab et al., 2023) foundation model. Despite these performance gains,

these frameworks still rely on generating a unified, full-resolution description field to maintain their accuracy.

Sparse deformable sampling provides a strategic alternative for improving efficiency. ALIKED (Zhao et al., 2023) introduces a dedicated sparse head that avoids the repetitive convolutions required by traditional methods on dense maps. This mechanism utilizes learnable offsets to gather information more flexibly than a fixed coordinate grid. Nevertheless, existing deformable approaches typically aggregate multi-scale features into a single dense representation before sampling occurs. This intermediate fusion step remains a bottleneck that impacts the overall inference throughput.

In this work, we introduce a description method that addresses these limitations by combining cross-layer deformable sampling with direct extraction from multiple feature scales. By decoupling sampling positions across the hierarchy, our approach generates highly expressive descriptors without the need to congregate features into a single volume. This strategy bypasses the construction of unified feature maps entirely, allowing our framework to preserve sharp structural details while maintaining a minimal memory footprint and high execution speed.

## 2.2 Deformable Operation

Deformable operations have become essential for modeling spatial transformations and geometric variations. Deformable Convolutional Networks (DCN) (Dai et al., 2017b) first introduced learnable offsets to adapt kernel receptive fields to complex object structures. Subsequent iterations (Zhu et al., 2019; Xiong et al., 2024) advanced these mechanisms by incorporating modulation components and hardware-efficient implementations. Deformable Attention (Xia et al., 2022) later extended these principles into the Transformer domain, enabling sparse and content-aware attention mechanisms. These developments provide the technical foundation for adaptive feature extraction in modern vision systems.

In the context of local feature learning, ASLFeat (Luo et al., 2020) introduced deformable convolutions within backbone layers to enhance the geometric invariance of keypoint representations. This architecture ensures that descriptors remain stable across significant image transformations. Building upon this, ALIKED (Zhao et al., 2023) integrates deformable modules within its feature extractor alongside a sparse sampling strategy. While this sampling head allows for more flexible feature gathering at specific interest

points, it remains dependent on a unified feature map generated through resource-intensive aggregation.

In contrast, our approach utilizes a streamlined backbone based on standard convolutions to prioritize inference throughput. We shift the focus from backbone deformation to the description stage through Cross-Layer Independent Deformable sampling. Unlike previous methods that sample from a single aggregated volume, our framework executes sparse fusion directly across multiple independent feature maps. By simultaneously performing offset prediction and feature extraction across different hierarchies, we achieve high matching precision while maintaining exceptional computational efficiency.

## 3 Cross-Layer Independent Deformable Description

In this section, we introduce the Cross-Layer Independent Deformable Description (CLIDD) method, as illustrated in Fig. 3, which generates highly discriminative descriptors through efficient cross-layer sparse sampling. We first describe the Cross-Layer Predictor, which coordinates precise sampling offsets by aggregating information across multiple feature scales. This is followed by the Layer-Independent Sampler, which extracts features from separate hierarchies using decoupled sampling points to capture multi-scale characteristics. Finally, we detail the kernel fusion techniques employed to optimize memory access patterns and ensure high-throughput inference for the entire module.

### 3.1 Cross-Layer Predictor

The CL-Predictor determines offsets by operating directly on feature vectors rather than processing dense, unified feature maps. For each keypoint, the predictor extracts a single feature vector from every available layer using normalized coordinates. These individual vectors are concatenated into a unified cross-layer embedding that represents the structural context across the hierarchy. This design bypasses the need for resizing or stacking large feature maps, which significantly reduces the computational and memory costs. By focusing operations on point-wise embeddings, the predictor removes the heavy overhead typically associated with dense grid calculations.

The concatenated embedding is processed through a point-wise convolution layer to generate a comprehensive set of sampling offsets. These offsets are partitioned into groups, providing each feature layer with its own

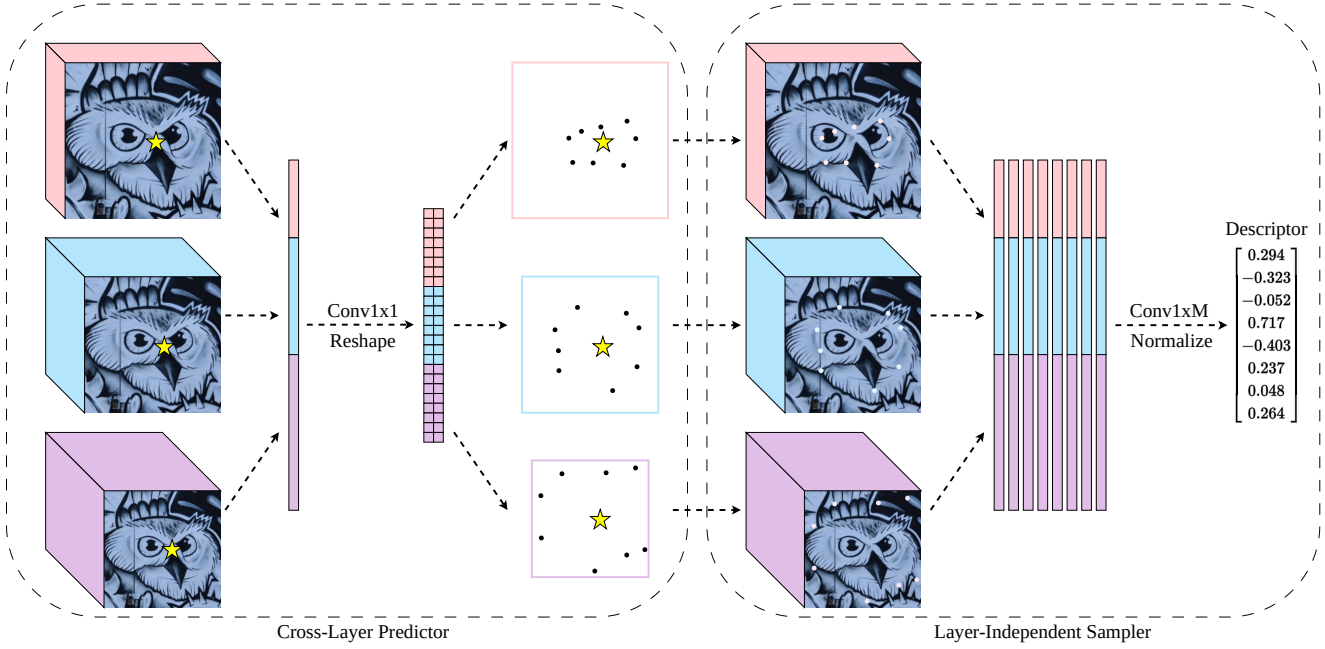


Fig. 3: **Mechanism of Cross-Layer Independent Deformable Description.** This framework facilitates sparse feature extraction across multiple hierarchies without relying on a unified dense feature map. The Cross-Layer Predictor utilizes spatially aligned embeddings to determine level-specific sampling offsets for each feature resolution. Guided by these offsets, the Layer-Independent Sampler performs decoupled feature retrieval from each layer, where  $M$  denotes the number of deformable sampling points per scale. This mechanism allows the model to capture both fine-grained geometry and semantic context simultaneously. The independently sampled features are then aggregated to produce a distinctive descriptor. While illustrated with three scales, this design is inherently scalable and generalizes to standard deformable sampling in single-layer configurations.

set of  $M$  unique coordinates. This coordinated prediction allows the model to leverage information from all scales to determine the most relevant sampling locations for each specific resolution. This strategy proves more effective than independent per-layer prediction while remaining significantly lighter than dense feature fusion. The CL-Predictor thus provides essential coordinate biases while maintaining a minimal computational footprint.

### 3.2 Layer-Independent Sampler

The LI-Sampler utilizes the specific offsets generated by the predictor to execute independent feature extraction across different hierarchies. Most traditional frameworks aggregate all feature levels into a single dense representation before any sampling occurs. Our approach avoids this fusion step entirely, which preserves the unique information present at each resolution level. By utilizing independent sampling offsets for each layer, the model gains the flexibility to capture diverse structural characteristics across the feature hierarchy. This ensures that the sampling process is not constrained

by a single, shared coordinate pattern across different scales.

Following the extraction, features from all layers are integrated into a final descriptor through a unified aggregation process. This method produces a more diverse representation of the local region compared to samplers relying on fixed or shared geometries. Although each layer employs its own specific offsets, the number of sampling points  $M$  remains constant, ensuring that the total computational cost does not scale with the complexity of the offsets. This decoupling of sampling positions allows the model to gather unique information across the hierarchy while keeping the overall system extremely fast and efficient.

### 3.3 Kernel Fusion and Efficient Implementation

Standard implementations of multi-scale description heads often encounter hardware bottlenecks due to excessive global memory operations. In a typical setup, sampled features from every layer are stored as intermediate tensors before the final aggregation. When processing a large number of feature points or using

high-dimensional feature layers, this approach creates substantial memory pressure. The frequent reading and writing of these intermediate results to global memory leads to severe latency penalties and limits the theoretical throughput of the model.

To overcome these architectural constraints, we implement a custom fused kernel that integrates feature sampling and aggregation into a single hardware operation. The kernel processes keypoints in small subsets, sampling the independent coordinates and performing partial aggregation directly within the fast on-chip SRAM. This design effectively decomposes the aggregation weight matrix into layer-wise components, allowing the contribution of each hierarchy to be computed locally. By eliminating the need to store large intermediate tensors in global memory, the fused implementation minimizes the peak memory footprint and significantly accelerates inference speed across various computational platforms.

## 4 Model Architecture and Training Scheme

This section details the architectural design and the training strategy of our framework. We first introduce a scalable architecture that integrates our core description method with optimized components to simultaneously achieve high-fidelity representation and fast inference. The training process then employs a composite objective function to optimize descriptor distinctiveness and geometric accuracy through metric learning and distillation. Finally, we provide the implementation details and training protocols that ensure robust performance across all model configurations.

### 4.1 Lightweight Model Architecture

We implement the proposed Cross-Layer Independent Deformable Description method as the core descriptor within a highly scalable network, as shown in Fig. 4. This design integrates a lightweight backbone and a streamlined detection head to achieve superior representation quality without compromising computational efficiency. The resulting architecture ensures robust performance across varying hardware constraints while maintaining the high throughput required for real-time deployment.

#### 4.1.1 Feature Backbone

Our framework employs a standardized encoder to generate a multi-scale feature hierarchy at 1/2, 1/8, and 1/32 downsampling ratios. The process initiates with

a  $4 \times 4$  convolution with a stride of 2 to reduce spatial resolution early and minimize initial computational overhead. At the 1/2 resolution stage, a single ResNet block (He et al., 2016) captures essential local details while maintaining a minimal memory footprint. Subsequent deeper stages utilize average pooling to reach 1/8 and 1/32 resolutions, allowing the capture of broader global context without excessive complexity.

We scale the number of residual blocks and channel widths at lower resolutions to balance semantic depth with execution speed. All configurations utilize ReLU activation functions to ensure the highest possible inference throughput on diverse hardware. The design deliberately keeps high-resolution stages shallow to avoid memory bottlenecks associated with processing large feature maps. This optimized multi-scale structure provides the necessary foundation for the subsequent detection and description tasks.

#### 4.1.2 Keypoint Detection Head

The detection head is standardized across all model tiers to operate at 1/2 resolution for an optimal balance between localization accuracy and efficiency. This module applies  $1 \times 1$  convolutions to the feature pyramid to compress channel dimensions before merging them through element-wise addition. This fusion mechanism efficiently integrates multi-scale context without increasing the total parameter count.

Following feature refinement through additional convolutional layers, a PixelShuffle operation restores the output to the original image dimensions. This technique eliminates upsampling artifacts and provides high-fidelity localization while avoiding the high computational cost of transposed convolutions. The unified head design ensures that even the largest models maintain real-time performance on resource-constrained platforms.

#### 4.1.3 Cross-Layer Independent Deformable Description Head

The description head utilizes the multi-scale hierarchy to construct final descriptors of dimension  $C_{desc}$ . At each detected keypoint, the cross-layer predictor identifies optimal sampling coordinates across the 1/2, 1/8, and 1/32 feature levels. This mechanism captures both structural details and broad semantic context without requiring resource-intensive upsampling layers. The layer-independent sampling strategy ensures that the resulting descriptors remain highly distinct and discriminative. This sparse extraction approach successfully preserves essential geometric features while by

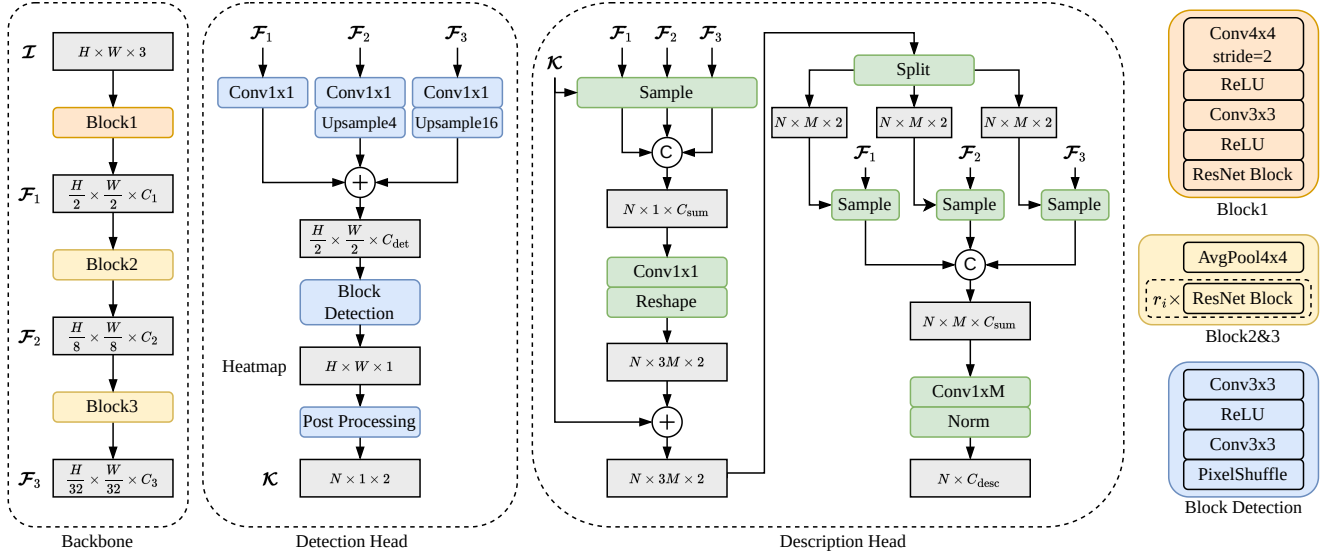


**Fig. 4: Model Architecture.** Our lightweight framework generates multi-scale representations using standard convolutional layers and ResNet blocks. The notation  $C_i$  for  $i \in \{1, 2, 3\}$  specifies the output channel counts for each feature block, while  $C_{\text{det}}$  and  $C_{\text{desc}}$  denote the dimensions for keypoint detection and final description. Within the description head, the total dimension of concatenated sampled features is defined as  $C_{\text{sum}} = C_1 + C_2 + C_3$ . Symbols  $\oplus$  and  $\odot$  indicate element-wise addition and concatenation operations, respectively. The term  $r_i$  for  $i \in \{2, 3\}$  determines the number of ResNet blocks within each specific stage. Following extraction, a post-processing module transforms the dense detection heatmap into sparse keypoints. By utilizing our Cross-Layer Independent Deformable Description method, the architecture produces high-quality descriptors without generating dense, high-resolution feature maps, thereby simultaneously enhancing both descriptive precision and computational efficiency.

passing the computational and memory bottlenecks of unified feature aggregation.

## 4.2 Loss Functions

Our framework is trained using image pairs with known geometric relationships to establish reliable ground-truth correspondences. The total training objective combines metric learning and knowledge distillation through three specific components: the DualSoftmax loss, the Orthogonal-Procrustes loss, and the Unfold-Softmax loss. Together, these functions optimize the feature discriminativeness and localization precision required for efficient keypoint extraction.

### 4.2.1 DualSoftmax Loss

The DualSoftmax loss provides the primary supervision for learning discriminative descriptors using image pairs  $\mathcal{I}_A$  and  $\mathcal{I}_B$  with known geometric relationships. For each training sample, we first extract 1024 keypoints from  $\mathcal{I}_A$  using the ALIKED-N32 (Zhao et al., 2023) method. The network then generates the corresponding descriptor matrix  $\mathbf{D}_A \in \mathbb{R}^{N \times C_{\text{desc}}}$  for these loca-

tions, where  $N$  denotes the total number of extracted descriptors. Using the known transformation between the pair, we warp the keypoint coordinates to  $\mathcal{I}_B$  and extract the paired descriptor matrix  $\mathbf{D}_B \in \mathbb{R}^{N \times C_{\text{desc}}}$ . Since some points may move outside the visible bounds of the second image, we define a binary visibility mask  $\mathbf{m} \in \{0, 1\}^N$  to identify valid correspondences.

To evaluate the similarity between the extracted feature sets, we compute the cosine distance matrix  $\mathbf{S} \in \mathbb{R}^{N \times N}$  as follows  $\mathbf{S} = \mathbf{D}_A \mathbf{D}_B^T$ . The matching probability matrix  $\mathbf{P}$  is then derived through a dual-softmax operation. This operation enforces mutual exclusivity by independently normalizing the similarity scores across both rows and columns:

$$\mathbf{P} = \text{softmax}_r\left(\frac{\mathbf{S}}{T}\right) \cdot \text{softmax}_c\left(\frac{\mathbf{S}}{T}\right), \quad (1)$$

where  $\text{softmax}_r$  and  $\text{softmax}_c$  denote the softmax functions applied along the rows and columns of the matrix respectively. A fixed temperature constant  $T = 20$  is utilized to concentrate the resulting probability distribution.

The DualSoftmax loss is formulated as the negative log-likelihood of the ground-truth matches:

$$L_{DS} = -\frac{1}{\mathbf{1}^T \mathbf{m}} \mathbf{m}^T \log \text{diag}(\mathbf{P}). \quad (2)$$

where  $\text{diag}(\cdot)$  extracts the diagonal elements, and  $\log(\cdot)$  denotes the element-wise logarithm. This objective constrains the embedding space to minimize the distance between corresponding features while effectively separating non-matching pairs. By optimizing this probability manifold, the network learns to produce highly unique feature representations. This process effectively maintains consistency between corresponding points while maximizing the variance between distinct regions.

#### 4.2.2 Orthogonal Procrustes Loss

Super-lightweight model configurations often require external guidance to realize their full discriminative potential. To address this, we employ knowledge distillation by supervising these efficient variants with a teacher model. We select ALIKED-N32 (Zhao et al., 2023) as the teacher architecture, which possesses a fixed descriptor dimension  $C'_{\text{teacher}}$  of 128. During training, we utilize the keypoint locations from the DualSoftmax phase to extract student descriptors  $\hat{\mathbf{D}}_A \in \mathbb{R}^{(B \cdot N) \times C_{\text{desc}}}$  and teacher descriptors  $\hat{\mathbf{D}}_{\text{teacher}} \in \mathbb{R}^{(B \cdot N) \times C'_{\text{teacher}}}$  across the batch. Because our student descriptors possess a lower dimensionality than those of the teacher ( $C_{\text{desc}} < C'_{\text{teacher}}$ ), we adopt the Orthogonal-Procrustes loss framework proposed in (Yao et al., 2025) for cross-dimensional distillation. A standard distillation target focuses on the internal distances within the embedding space, defined as:

$$\|\hat{\mathbf{D}}_A \hat{\mathbf{D}}_A^T - \hat{\mathbf{D}}_{\text{teacher}} \hat{\mathbf{D}}_{\text{teacher}}^T\|_F^2. \quad (3)$$

However, this formulation lacks direct geometric alignment. To distill the geometric structure more effectively, we follow (Yao et al., 2025) and apply a Low-Rank Approximation (LRA) to compress the rank of  $\hat{\mathbf{D}}_{\text{teacher}} \hat{\mathbf{D}}_{\text{teacher}}^T$  to  $C_{\text{desc}}$ . We compute the Singular Value Decomposition (SVD) of the teacher descriptors as  $\hat{\mathbf{D}}_{\text{teacher}} = \mathbf{U} \Sigma \mathbf{V}^T$ . We then construct the compressed descriptors using the leading  $C_{\text{desc}}$  singular vectors and values, denoted as  $\hat{\mathbf{D}}_l = \mathbf{U}_C \Sigma_C$ . Since the number of points  $N$  consistently exceeds the feature dimension  $C_{\text{desc}}$ , this compression is inherently lossy. To accelerate training, we perform this LRA per batch rather than per individual image. Crucially, as lossy compression does not preserve unit length, we normalize  $\hat{\mathbf{D}}_l$  along the feature dimension to ensure its row

vectors return to the unit hypersphere, denoted as  $\hat{\mathbf{D}}_n$ . The distillation objective is subsequently updated as:

$$\|\hat{\mathbf{D}}_A \hat{\mathbf{D}}_A^T - \hat{\mathbf{D}}_n \hat{\mathbf{D}}_n^T\|_F^2. \quad (4)$$

The optimal solution seeks a transformation  $\hat{\mathbf{D}}_A^* = \hat{\mathbf{D}}_n \mathbf{X}$  where  $\mathbf{X}$  belongs to the Orthogonal group  $\mathbb{O}(C_{\text{desc}}, \mathbb{R})$ . We identify the optimal orthogonal matrix  $\Omega$  by solving the Orthogonal-Procrustes Problem (OPP) (Schönemann, 1966):

$$\begin{aligned} \Omega &= \arg \min_{\mathbf{X} \in \mathbb{O}(C_{\text{desc}}, \mathbb{R})} \|\hat{\mathbf{D}}_l \mathbf{X} - \hat{\mathbf{D}}_A\|_F^2 \\ &= \arg \max_{\mathbf{X} \in \mathbb{O}(C_{\text{desc}}, \mathbb{R})} \text{tr}(\hat{\mathbf{D}}_A^T \hat{\mathbf{D}}_l \mathbf{X}) \\ &= \mathbf{V}_p \mathbf{U}_p^T, \end{aligned} \quad (5)$$

where  $\mathbf{U}_p \Sigma_p \mathbf{V}_p^T$  is the SVD of the correlation matrix  $\hat{\mathbf{D}}_A^T \hat{\mathbf{D}}_l$ . The final Orthogonal-Procrustes loss is formulated as:

$$L_{OP} = \|1 - \text{diag}(\hat{\mathbf{D}}_n \Omega \hat{\mathbf{D}}_A^T)\|_F^2. \quad (6)$$

Through this scheme, our compact models effectively inherit the robust representational properties encoded by high-capacity teacher architectures. While this batch-wise formulation differs from the lossless compression in (Yao et al., 2025), executing SVD operations per batch significantly accelerates training. The integration of DualSoftmax ensures the model maintains high accuracy despite the lossy nature of the compressed target. Furthermore, the simultaneous integration of DualSoftmax supervision provides robust discriminative guidance, ensuring that the model maintains high matching accuracy despite the lossy nature of the compressed distillation target.

#### 4.2.3 UnfoldSoftmax Loss

The detection training aims to achieve precise keypoint localization while ensuring that the resulting inference remains computationally efficient. We supervise the raw output logits directly to enable the network to produce discriminative response maps without additional activation layers. This approach ensures reliable keypoint localization while maintaining a lean execution profile for deployment.

We implement the UnfoldSoftmax loss  $L_{US}$  following the distillation framework proposed in (Yao et al., 2025). This methodology leverages the ALIKED-N32 model to provide high-quality detection labels on image  $\mathcal{I}_A$  for supervision. The training process effectively treats local neighborhood patches as competitive classification tasks to refine keypoint precision. We utilize efficient convolutional operations to compute this

Table 1: **Network configurations.** We denote the models as A/N/T/S/M/L/G/E/U to indicate the model size.

Model	Network Configuration							Params (MP)				
	$C_1$	$C_2$	$C_3$	$r_2$	$r_3$	$C_{\text{det}}$	$M$	$C_{\text{desc}}$	Backbone	Detect	Desc	Total
A48(Atom)	4	4	4	1	1	4	4	48	0.00123	0.00036	0.003	0.004
N64(Nano)	8	8	8	1	1	8	8	64	0.00448	0.00109	0.014	0.019
T64(Tiny)	8	16	24	1	1	8	8	64	0.015	0.00128	0.027	0.043
S64(Small)	8	24	32	1	1	8	16	64	0.026	0.00141	0.072	0.100
M64(Medium)	16	32	48	1	1	8	16	64	0.058	0.00167	0.108	0.168
L64(Large)	16	48	96	1	1	8	16	64	0.166	0.00218	0.179	0.347
G128(Giant)	16	64	256	1	1	8	32	128	0.809	0.00359	1.441	2.254
E128(Enormous)	16	64	256	2	2	8	32	128	2.063	0.00359	1.441	3.508
U128(Ultra)	32	128	256	2	2	8	32	128	2.612	0.00423	1.784	4.400

Table 2: **Loss weighting configurations.** The table details the coefficients  $w_{\text{DS}}$ ,  $w_{\text{OP}}$ , and  $w_{\text{US}}$  assigned to each model architecture during training.

Model	$w_{\text{DS}}$	$w_{\text{OP}}$	$w_{\text{US}}$
A48	0.05	1	1
N64	0.1	1	1
T64	0.5	1	1
S64	1	0	1
M64	1	0	1
L64	1	0	1
G128	1	0	1
E128	1	0	1
U128	1	0	1

loss, which ensures numerical stability without increasing the memory footprint. This strategy allows the lightweight detector to inherit the robust localization capabilities of the teacher model while remaining optimized for real-time performance.

### 4.3 Implementation Details

We provide nine model configurations ranging from Atom (A) to Ultra (U) to address diverse application scenarios, as detailed in Table 1. The scaling logic for these variants prioritize increasing capacity in deeper feature layers where spatial dimensions are smaller. Specifically, the 1/2 resolution stage is restricted to a maximum of 32 channels and a single ResNet block to prevent high-resolution layers from becoming speed bottlenecks. Simultaneously, the keypoint detection head maintains a narrow width of 8 channels to maximize throughput on large-scale feature maps. The description head also scales the number of sampling offsets  $M$  from 4 up to 32 as the model capacity grows. This architectural approach ensures extreme efficiency, resulting in a minimal footprint of only 4,252 parameters for the Atom48 variant.

The training objective is defined as a weighted combination of the three loss functions:

$$L_{\text{total}} = w_{\text{DS}}L_{\text{DS}} + w_{\text{OP}}L_{\text{OP}} + w_{\text{US}}L_{\text{US}}. \quad (7)$$

The specific weighting coefficients vary according to the model scale as specified in Table 2. For the more compact architectures, we utilize the  $L_{\text{OP}}$  term to facilitate knowledge distillation. We systematically reduce the weight of the direct metric learning loss  $w_{\text{DS}}$  as the model scale decreases to prioritize the distillation signal. This strategy ensures that smaller configurations effectively inherit the representational quality of higher-capacity models.

Our training process utilizes the MegaDepth (Li and Snavely, 2018) dataset alongside sampled subsets of ScanNet (Dai et al., 2017a) and Revisitop1m (Radenović et al., 2018). We strictly exclude scenes from the MegaDepth-1500 test set to prevent data leakage and ensure fair evaluation. For datasets without ground-truth transformations, we construct training pairs using synthetic homography transformations and apply color augmentation to all  $640 \times 640$  input images. The network is optimized using the AdamW (Loshchilov, 2017) optimizer for three epochs with an initial learning rate of 0.002. This learning rate is halved after each epoch to refine model convergence. All models are trained on four L40S GPUs, with even the largest U128 configuration requiring only one hour to complete.

## 5 Experiments

In this section, we first analyze the computational efficiency of our method under the constraints of onboard deployment. We then conduct a comprehensive comparison against state-of-the-art (SOTA) methods across several benchmarks, including homography estimation, relative pose estimation, and visual localization. A series of ablation studies verifies the impact of our architectural design, training strategy, and the efficiency gains from our fused kernel implementation. We also

investigate the discriminative power of our descriptors across varying spatial densities to assess robustness under high-density sampling conditions.

We benchmark our approach against a diverse set of SOTA methods, including SuperPoint (DeTone et al., 2018), DISK (Tyszkiewicz et al., 2020), ALIKED (Zhao et al., 2023), and AWDesc (Wang et al., 2023). For the DeDoDe (Edstedt et al., 2024a) series, we utilize the improved detector from DeDoDe-v2 (Edstedt et al., 2024b) to generate keypoints. Our evaluation also incorporates efficiency-oriented models such as XFeat (Potje et al., 2024), EdgePoint (Yao et al., 2024), and EdgePoint2 (Yao et al., 2025).

Unless otherwise specified, we extract 4096 keypoints per image for all evaluated methods to ensure a fair comparison. A Non-Maximum Suppression (NMS) radius of 2 pixels is applied to our method to maintain a balanced spatial distribution. We employ a dual-softmax matcher with a confidence threshold of 0.01 for our models and DeDoDe, following the setup in (Edstedt et al., 2024a). The remaining baseline methods utilize the Mutual-Nearest Neighbor matching strategy as their standard default configuration.

To reach the hardware efficiency targets discussed in Section 3.3, we implement our custom fused kernels in both Triton and CUDA. This specialized implementation enables our method to achieve the reported throughput and latency during evaluation. These optimizations ensure that the computational benefits of our architectural design are fully realized in the practical deployment scenarios analyzed across the following benchmarks.

### 5.1 Runtime Efficiency

**Setup** We analyze several efficiency metrics, including descriptor dimensionality (Dim), millions of parameters (MP), and computational complexity (GFLOPs). Furthermore, we evaluate the execution speed on an NVIDIA Jetson Orin-NX, which serves as a standard embedded platform for edge applications. All neural networks are deployed and measured using TensorRT to maximize performance on the integrated GPU. This assessment focuses on throughput measured in frames per second (FPS) for a standard  $480 \times 640$  input resolution with 1024 extracted keypoints, following the protocol in (Zhao et al., 2023).

**Results** The results in Table 3 demonstrate that our method significantly outperforms all compared baselines in terms of both memory footprint and runtime efficiency. Our most lightweight configuration, Ours-A48, requires only 4252 (0.004M) parameters and

0.08 GFLOPs, representing the smallest model size among all tested methods. Despite its minimal resource consumption, it achieves a throughput of over 880 FPS. Even as the model capacity increases, our larger variants maintain competitive performance across the board.

Compared to established lightweight benchmarks like XFeat and EdgePoint2, our models provide a more efficient scaling of descriptor dimensions relative to processing speed. For example, Ours-U128 delivers high-capacity 128-dimensional descriptors while maintaining a frame rate of 281.4 FPS. This throughput is notably higher than many smaller-scale models such as ALIKED and AWDesc. These results highlight the effectiveness of our architectural design and implementation in maximizing hardware utilization for real-time onboard scenarios.

### 5.2 Homography Estimation

**Setup** The HPatches (Balntas et al., 2017) dataset provides 116 sequences characterized by diverse illumination and viewpoint changes. Following established conventions (Zhao et al., 2022; Dusmanu et al., 2019), we exclude eight unreliable scenes and employ mutual nearest neighbor matching. We then utilize MAGSAC++ (Barath et al., 2020) for robust homography estimation between image pairs. Performance is measured using Mean Homography Accuracy (MHA) at error thresholds of 1, 3, and 5 pixels. This metric represents the percentage of correctly projected image corners relative to the ground truth homography.

**Results** The evaluation on the HPatches dataset in Table 4 reveals that our method achieves leading homography accuracy across all error thresholds. Within the compact category, our models consistently outperform established lightweight descriptors such as XFeat, EdgePoint, and variants of EdgePoint2. Notably, even the entry-level Ours-A48 variant exceeds several baselines in precision while utilizing only 0.004 million parameters. This advantage is particularly evident at the strictest 1-pixel threshold, where our configurations maintain significantly higher accuracy under complex conditions.

In the standard category, our high-capacity variants demonstrate a clear performance lead over established benchmarks such as DISK and ALIKED. Our approach also maintains a competitive edge against significantly heavier frameworks, including DeDoDe and AWDesc. These results demonstrate that our framework achieves superior accuracy while providing a clear efficiency advantage over existing high-performance methods. The

Table 3: **Computation Resources Comparison.** Our methods achieve superior throughput and resource efficiency for edge applications. The best results are marked as **bold**.

Standard	Method	Dim	MP	GFLOPs	FPS
Standard	SuperPoint (DeTone et al., 2018)	256	1.301	26.11	124.2
	DISK (Tyszkiewicz et al., 2020)	128	1.092	98.97	26.9
	ALIKED-T16 (Zhao et al., 2023)	64	0.192	1.37	52.5
	ALIKED-N16 (Zhao et al., 2023)	128	0.677	4.05	31.4
	ALIKED-N32 (Zhao et al., 2023)	128	0.980	4.62	29.7
	AWDesc-T16 (Wang et al., 2023)	128	0.172	4.50	180.4
	AWDesc-T32 (Wang et al., 2023)	128	0.390	11.81	168.2
	AWDesc-CA (Wang et al., 2023)	128	10.13	27.45	84.0
	DeDoDe-B (Edstedt et al., 2024b)	256	29.93	315.58	5.27
	DeDoDe-G (Edstedt et al., 2024b)	256	342.0	323.74	2.71
Fast	XFeat (Potje et al., 2024)	64	0.658	1.31	277.4
	EdgePoint (Yao et al., 2024)	32	0.030	0.36	838.8
	EdgePoint2-T48 (Yao et al., 2025)	48	0.028	0.50	503.0
	EdgePoint2-M64 (Yao et al., 2025)	64	0.089	1.22	437.2
	EdgePoint2-E64 (Yao et al., 2025)	64	0.155	1.96	375.7
	Ours-A48	48	<b>0.004</b>	<b>0.08</b>	<b>881.1</b>
	Ours-N64	64	0.019	0.26	842.7
	Ours-T64	64	0.043	0.29	803.5
	Ours-S64	64	0.100	0.35	746.4
	Ours-M64	64	0.168	0.86	625.1
	Ours-L64	64	0.347	1.03	591.4
	Ours-G128	128	2.254	2.60	475.4
	Ours-E128	128	3.508	3.31	431.3
	Ours-U128	128	4.400	7.12	281.4

Table 4: **Homography estimation on HPatches.**

The top three best results in each sector are highlighted in red, green and blue.

Standard	Method	MHA		
		@1	@3	@5
Compact	ALIKED-T16 (Zhao et al., 2023)	50.74	83.89	90.56
	XFeat (Potje et al., 2024)	47.04	80.19	89.07
	EdgePoint (Yao et al., 2024)	47.96	78.89	87.04
	EdgePoint2-T48 (Yao et al., 2025)	50.19	81.48	88.89
	EdgePoint2-M64 (Yao et al., 2025)	53.70	82.96	89.63
	EdgePoint2-E64 (Yao et al., 2025)	53.33	82.78	90.56
	Ours-A48	49.81	82.22	88.89
	Ours-N64	<b>54.63</b>	81.85	88.89
	Ours-T64	52.22	84.26	90.93
	Ours-S64	54.07	<b>84.81</b>	<b>91.11</b>
Standard	Ours-M64	<b>56.11</b>	<b>84.81</b>	<b>91.11</b>
	Ours-L64	<b>55.37</b>	<b>84.44</b>	<b>92.04</b>
	SuperPoint (DeTone et al., 2018)	49.81	81.48	88.89
	DISK (Tyszkiewicz et al., 2020)	51.30	79.44	88.33
	ALIKED-N16 (Zhao et al., 2023)	51.67	83.89	90.37
	ALIKED-N32 (Zhao et al., 2023)	50.37	83.52	90.74
	AWDesc-T16 (Wang et al., 2023)	53.89	83.33	90.56
	AWDesc-T32 (Wang et al., 2023)	56.67	<b>85.19</b>	90.37
	AWDesc-CA (Wang et al., 2023)	54.07	<b>85.00</b>	<b>92.41</b>
	DeDoDe-B (Edstedt et al., 2024a)	55.56	83.33	89.44
	DeDoDe-G (Edstedt et al., 2024a)	55.93	83.33	90.93
	Ours-G128	<b>58.15</b>	<b>85.00</b>	<b>91.11</b>
	Ours-E128	<b>57.04</b>	84.63	<b>92.04</b>
	Ours-U128	<b>56.85</b>	<b>86.30</b>	90.74

consistent ranking of our various configurations across both categories validates the overall reliability of our method for diverse homography estimation tasks.

### 5.3 Relative Pose Estimation

**Setup** The MegaDepth-1500 (Li and Snavely, 2018) and ScanNet-1500 (Dai et al., 2017a) datasets are employed to assess matching robustness under varying viewpoints and illumination in outdoor and indoor scenes. Additionally, the Image Matching Challenge 2022 (IMC2022) (Howard et al., 2022) serves as a specialized outdoor benchmark for evaluating fundamental matrix estimation.

Regarding experimental configurations, images are resized to a maximum dimension of 1200 pixels for MegaDepth and  $480 \times 640$  for ScanNet. We follow the matching protocols established in (Sun et al., 2021; Wang et al., 2024b) and utilize LO-RANSAC (Larsen and contributors, 2020) for essential and fundamental matrix estimation. Optimal matching thresholds for each method are determined according to the strategy in (Potje et al., 2024). Performance is measured using the Area Under the Curve (AUC) for pose accuracy at thresholds of  $5^\circ$ ,  $10^\circ$ , and  $20^\circ$ . For IMC2022, images are resized to  $800 \times 800$  and we utilize MAGSAC++ (Barath et al., 2020) for robust estimation. The mean Average Accuracy (mAA) is adopted as the primary metric for both private and public subsets.

**Results** The relative pose estimation results on MegaDepth-1500, ScanNet-1500, and IMC2022 are summarized in Table 5. For the outdoor MegaDepth-

Table 5: **Relative pose estimation on MegaDepth-1500, ScanNet-1500 and IMC2022.** The top three best results of each sector are marked as red, green and blue.

Method	MegaDepth-1500			ScanNet-1500			IMC2022		
	AUC@5°	AUC@10°	AUC@20°	AUC@5°	AUC@10°	AUC@20°	Private	Public	
Compact	ALIKED-T16 (Zhao et al., 2023)	<b>58.46</b>	<b>70.89</b>	<b>79.77</b>	14.10	27.18	40.54	0.542	0.559
	XFeat (Potje et al., 2024)	43.61	56.78	67.38	12.14	25.08	39.72	0.489	0.505
	EdgePoint (Yao et al., 2024)	42.92	55.72	66.04	11.31	23.46	36.59	0.436	0.460
	EdgePoint2-T48 (Yao et al., 2025)	48.71	60.94	70.67	13.72	27.20	42.01	0.550	0.564
	EdgePoint2-M64 (Yao et al., 2025)	53.20	65.17	74.05	15.28	29.95	44.89	0.608	0.615
	EdgePoint2-E64 (Yao et al., 2025)	54.32	66.29	75.38	16.20	31.32	46.63	0.625	0.632
	Ours-A48	44.98	57.13	66.41	12.62	25.35	39.23	0.473	0.492
	Ours-N64	53.91	65.81	75.12	14.88	29.34	44.35	0.583	0.588
	Ours-T64	54.26	66.74	76.16	15.33	31.03	47.37	0.577	0.597
	Ours-S64	55.43	67.74	77.28	<b>16.74</b>	<b>31.96</b>	<b>47.77</b>	<b>0.603</b>	<b>0.605</b>
Standard	Ours-M64	<b>57.41</b>	<b>69.81</b>	<b>78.62</b>	<b>17.28</b>	<b>33.55</b>	<b>49.36</b>	<b>0.602</b>	<b>0.605</b>
	Ours-L64	<b>58.29</b>	<b>70.83</b>	<b>80.02</b>	<b>17.86</b>	<b>33.59</b>	<b>49.33</b>	<b>0.619</b>	<b>0.617</b>
	SuperPoint (DeTone et al., 2018)	43.52	56.51	66.78	14.67	28.97	43.76	0.475	0.485
	DISK (Tyszkiewicz et al., 2020)	54.68	66.63	75.42	13.61	26.31	39.75	0.601	0.589
	ALIKED-N16 (Zhao et al., 2023)	57.62	70.00	79.05	13.16	25.90	39.90	0.630	0.632
	ALIKED-N32 (Zhao et al., 2023)	61.10	73.56	82.16	12.72	24.65	37.05	0.626	0.624
	AWDesc-T16 (Wang et al., 2023)	48.90	61.27	70.41	14.72	29.41	43.55	0.553	0.574
	AWDesc-T32 (Wang et al., 2023)	51.26	63.84	72.76	16.79	32.12	47.29	0.583	0.597
	AWDesc-CA (Wang et al., 2023)	53.89	66.66	75.87	16.61	32.05	47.00	0.581	0.595
	DeDoDe-B (Edstedt et al., 2024a)	59.56	71.14	79.41	16.75	30.93	44.43	0.623	0.617
	DeDoDe-G (Edstedt et al., 2024a)	<b>63.73</b>	<b>76.13</b>	<b>84.91</b>	<b>19.97</b>	<b>37.32</b>	<b>53.39</b>	0.673	0.667
Ours	Ours-G128	62.22	74.61	83.08	<b>18.52</b>	35.04	51.85	<b>0.689</b>	<b>0.686</b>
	Ours-E128	<b>62.84</b>	<b>75.16</b>	<b>83.72</b>	18.35	<b>35.38</b>	<b>51.97</b>	<b>0.695</b>	<b>0.694</b>
	Ours-U128	<b>64.75</b>	<b>77.15</b>	<b>85.77</b>	<b>18.94</b>	<b>36.46</b>	<b>53.66</b>	<b>0.717</b>	<b>0.716</b>

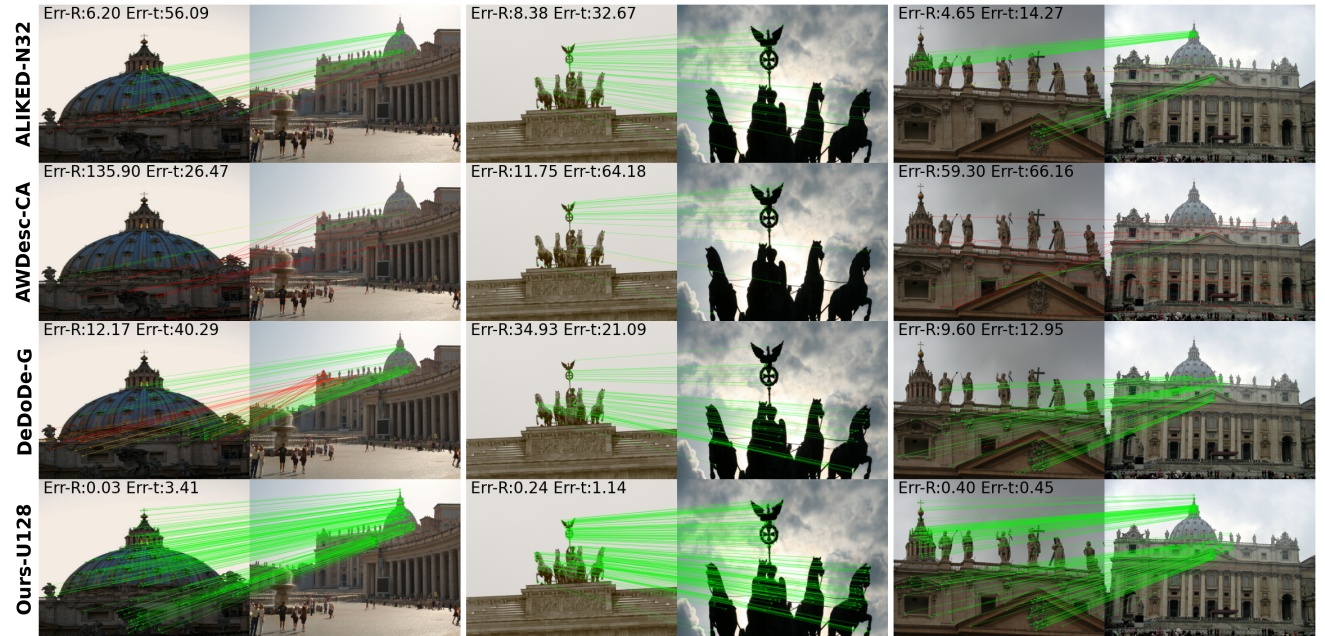


Fig. 5: **Qualitative results on MegaDepth-1500.** We compare ALIKED-N32, AWDesc-CA and DeDoDe-G against our U128 model.

1500 benchmark, our models demonstrate exceptional accuracy across various conditions. In the compact category, our variants consistently outperform XFeat (Potje et al., 2024), EdgePoint (Yao et al., 2024), and EdgePoint2 (Yao et al., 2025) across all AUC thresholds. Among standard descriptors, our high-capacity models achieve the top rankings, surpassing established frame-

works such as DeDoDe-G (Edstedt et al., 2024a) and ALIKED (Zhao et al., 2023). This performance indicates that our features are highly robust to the significant viewpoint and illumination changes typical of outdoor environments.

The relative pose estimation results on MegaDepth-1500, ScanNet-1500, and IMC2022 are summarized in

**Table 5.** For the outdoor MegaDepth-1500 benchmark, our models demonstrate exceptional accuracy across various conditions. In the compact category, our variants consistently outperform XFeat (Potje et al., 2024), EdgePoint (Yao et al., 2024), and EdgePoint2 (Yao et al., 2025) across all AUC thresholds. Among standard descriptors, our high-capacity models achieve the top rankings, surpassing established frameworks such as DeDoDe-G (Edstedt et al., 2024a) and ALIKED (Zhao et al., 2023). This performance indicates that our features are highly robust to the significant viewpoint and illumination changes typical of outdoor environments.

The evaluation on IMC2022 further confirms the superiority of our framework for fundamental matrix estimation. Our standard models achieve the highest mean Average Accuracy on both private and public subsets, notably outperforming previous state-of-the-art results from DeDoDe-G (Edstedt et al., 2024a). Similarly, our compact variants maintain a high ranking, with many configurations rivaling the performance of standard-sized descriptors. This outcome validates the high discriminative power of our features even under the rigorous requirements of large-scale competition benchmarks.

Overall, the experimental results demonstrate that our framework achieves state-of-the-art precision while providing a substantial efficiency advantage. By employing a standard CNN architecture, our U128 model surpasses the DINOv2-based DeDoDe-G (Edstedt et al., 2024a) in accuracy with a compact 128-dimensional descriptor and less than 1% of the parameters. Simultaneously, our ultra-lightweight A48 variant achieves matching performance comparable to SuperPoint (DeTone et al., 2018) while utilizing only approximately 0.3% of its parameter count. This massive reduction in resource overhead confirms that our architecture successfully delivers superior accuracy while maintaining the exceptional efficiency required for real-time deployment.

## 5.4 Visual Localization

**Setup** The visual localization performance is evaluated using the Aachen Day-Night v1.1 (Sattler et al., 2018) and InLoc (Taira et al., 2018) datasets to assess robustness against extreme day-night illumination changes and complex indoor environments. We integrate our descriptors into the Hierarchical Localization framework (Sarlin et al., 2019) following the standard pipeline for feature extraction and matching. In accordance with recommended protocols, images are resized to a maximum dimension of 1024 pixels for Aachen and

1600 pixels for InLoc. Accuracy is quantified by the percentage of successfully localized images within translation and rotation thresholds of (0.25m, 2°), (0.5m, 5°), and (5m, 10°).

**Results** The visual localization results are presented in Table 6. On the Aachen Day-Night benchmark, our framework consistently achieves top-tier accuracy across both day and night conditions. Our compact models provide robustness that rivals many standard-sized methods. Meanwhile, our standard variants remain highly competitive against established pipelines such as ALIKED (Zhao et al., 2023) and DISK (Tyszkiewicz et al., 2020). These results indicate that our descriptors are exceptionally stable under the extreme illumination transitions characteristic of day-night cycles.

For the indoor InLoc dataset, our approach demonstrates a clear performance advantage in environments with significant viewpoint changes. In the standard sector, our models occupy leading positions across nearly all thresholds for both DUC1 and DUC2 subsets. This performance notably exceeds other high-capacity methods like AWDesc (Wang et al., 2023) and DeDoDe (Edstedt et al., 2024a), the latter of which shows more limited generalization to these indoor scenes. The superior results on InLoc underscore the high discriminative power and geometric consistency of our learned features.

Overall, these experiments confirm that our framework delivers state-of-the-art localization precision across diverse and challenging environments. This consistent performance across outdoor illumination changes and indoor geometric variations validates the effectiveness of our approach. Our framework remains ideal for practical applications requiring both high reliability and real-time processing speeds.

## 5.5 Ablation Study

### 5.5.1 Design of the CLIDD

We evaluate the internal components of CLIDD by analyzing the design of the Predictor and Sampler. As shown in Table 7, our sparse extraction strategy is compared against several internal baselines using the MegaDepth-1500 and ScanNet-1500 benchmarks. The results demonstrate that the Cross-Layer Predictor outperforms configurations utilizing only a single feature resolution. Similarly, the Layer-Independent Sampler yields higher precision than coupled sampling alternatives. Integrating both components maximizes geometric robustness and discriminative power. These gains

Table 6: **Visual localization on Aachen Day-Night v1.1 and InLoc.** The top three best results of each sector are marked as red, green and blue.

Method	Aachen Day-Night v1.1										InLoc				
	Day					Night					DUC1			DUC2	
	0.25m 2°	0.5m 5°	5m 10°	0.25m 2°	0.5m 5°	5m 10°	0.25m 2°	0.5m 5°	5m 10°	0.25m 2°	0.5m 5°	5m 10°	0.25m 2°	0.5m 5°	5m 10°
Compact	ALIKED-T16 (Zhao et al., 2023)	<b>89.1</b>	<b>95.0</b>	98.2	<b>77.5</b>	<b>91.1</b>	<b>99.0</b>	33.8	49.0	59.1	33.6	49.6	57.3		
	XFeat (Potje et al., 2024)	86.0	93.9	97.6	70.7	85.9	97.9	36.4	54.0	64.1	30.5	44.3	57.3		
	EdgePoint (Yao et al., 2024)	86.9	93.2	97.6	66.0	85.9	95.3	28.3	43.4	53.0	22.9	37.4	49.6		
	EdgePoint2-T48 (Yao et al., 2025)	86.8	94.1	98.1	74.9	87.4	97.9	34.8	48.5	61.6	37.4	55.7	65.6		
	EdgePoint2-M64 (Yao et al., 2025)	87.1	94.7	98.2	75.9	90.1	<b>99.0</b>	<b>37.9</b>	<b>57.1</b>	<b>68.7</b>	39.7	<b>60.3</b>	<b>66.4</b>		
	EdgePoint2-E64 (Yao et al., 2025)	86.9	<b>95.0</b>	<b>98.3</b>	<b>77.0</b>	<b>91.6</b>	<b>99.0</b>	36.4	54.5	66.2	<b>41.2</b>	<b>58.8</b>	<b>67.2</b>		
	Ours-A48	86.9	94.5	97.7	72.8	85.3	95.8	28.8	43.9	53.5	28.2	43.5	55.0		
	Ours-N64	<b>89.1</b>	<b>95.0</b>	98.2	74.3	88.5	<b>99.0</b>	35.9	50.0	63.1	36.6	52.7	62.6		
	Ours-T64	88.7	94.8	<b>98.3</b>	72.8	90.1	<b>99.0</b>	35.4	55.6	64.6	38.9	52.7	65.6		
	Ours-S64	88.8	94.8	<b>98.4</b>	75.4	90.1	<b>99.0</b>	35.4	52.0	65.2	<b>40.5</b>	58.0	65.6		
	Ours-M64	<b>89.4</b>	<b>95.3</b>	98.2	75.9	90.1	<b>99.0</b>	<b>37.4</b>	<b>56.1</b>	<b>67.2</b>	39.7	55.0	63.4		
	Ours-L64	88.3	<b>95.0</b>	<b>98.3</b>	<b>78.0</b>	<b>90.6</b>	<b>99.0</b>	<b>38.4</b>	<b>56.6</b>	<b>68.2</b>	<b>40.5</b>	<b>61.1</b>	<b>67.9</b>		
Standard	SuperPoint (DeTone et al., 2018)	88.3	94.4	98.1	69.1	85.9	95.8	33.3	50.0	59.6	32.8	51.9	63.4		
	DISK (Tyszkiewicz et al., 2020)	87.3	95.5	98.5	<b>78.0</b>	89.0	99.0	35.9	53.0	66.2	24.4	40.5	57.3		
	ALIKED-N16 (Zhao et al., 2023)	88.8	<b>96.1</b>	<b>98.8</b>	74.3	89.5	99.0	32.8	54.0	65.7	35.1	50.4	58.0		
	ALIKED-N32 (Zhao et al., 2023)	86.4	95.3	98.3	74.9	90.1	<b>99.5</b>	36.9	51.0	66.7	35.9	49.6	64.1		
	AWDesc-T16 (Wang et al., 2023)	<b>89.2</b>	95.1	98.4	75.4	88.0	96.9	38.9	56.1	66.7	35.1	51.9	64.9		
	AWDesc-T32 (Wang et al., 2023)	88.2	<b>95.9</b>	98.4	<b>77.0</b>	90.1	98.4	38.4	57.6	68.7	34.4	55.7	65.6		
	AWDesc-CA (Wang et al., 2023)	88.5	95.4	98.4	74.9	<b>91.1</b>	99.0	39.9	<b>60.1</b>	<b>71.2</b>	42.7	58.0	<b>68.7</b>		
	DeDoDe-B (Edstedt et al., 2024a)	86.5	95.0	98.2	74.9	89.0	<b>99.5</b>	29.8	43.4	51.5	19.8	30.5	41.2		
	DeDoDe-G (Edstedt et al., 2024a)	88.0	95.4	98.5	74.3	<b>90.6</b>	<b>99.5</b>	38.9	57.6	68.7	29.8	46.6	54.2		
	Ours-G128	88.8	95.6	<b>98.7</b>	75.4	90.1	99.0	<b>41.9</b>	<b>61.1</b>	<b>71.2</b>	<b>47.3</b>	<b>64.1</b>	<b>69.5</b>		
	Ours-E128	<b>89.0</b>	95.6	<b>98.7</b>	<b>78.5</b>	<b>90.6</b>	99.0	<b>41.4</b>	59.6	70.2	<b>45.0</b>	<b>64.1</b>	<b>70.2</b>		
	Ours-U128	<b>89.4</b>	<b>95.8</b>	<b>98.8</b>	76.4	<b>91.1</b>	99.0	<b>43.4</b>	<b>62.1</b>	<b>71.7</b>	<b>45.8</b>	<b>61.1</b>	67.9		

Table 7: **Ablation study of specific structural configurations.** These experiments compare single-layer versus cross-layer aggregation for offset prediction and shared versus layer-independent strategies for feature sampling.

Model	Predictor	Sampler	MegaDepth-1500			ScanNet-1500		
			AUC@5°	AUC@10°	AUC@20°	AUC@5°	AUC@10°	AUC@20°
A48	Single	Independent	42.56	54.27	63.93	12.41	25.19	38.92
	Cross	Independent	<b>44.98</b>	<b>57.13</b>	<b>66.41</b>	<b>12.62</b>	<b>25.35</b>	<b>39.23</b>
	Cross	Shared	43.20	55.22	64.72	12.15	24.41	37.82
U128	Single	Independent	63.17	75.51	84.14	18.69	35.91	52.74
	Cross	Independent	<b>64.75</b>	<b>77.15</b>	<b>85.77</b>	<b>18.94</b>	<b>36.46</b>	<b>53.66</b>
	Cross	Shared	63.43	75.80	84.38	18.14	35.04	52.02

remain consistent across both the lightweight A48 and high-capacity U128 variants, confirming the architectural scalability of our approach.

### 5.5.2 Comparison with Dense Description Head

We evaluate CLIDD against description methods requiring dense feature fusion. As shown in Table 8, both sub-scale and full-scale vanilla strategies exhibit limited effectiveness when applied to the ultra-lightweight A48 backbone. While scaling up to the high-capacity U128 model improves accuracy, the results remain inferior to our CLIDD-based approach. We also observe that the full-scale strategy imposes significant memory pressure during training, requiring more than double the GPU memory per card compared to our method. To accommodate these intensive resource demands, we reduce

the training batch size to one-fourth of the original configuration and employ gradient accumulation. Despite these adjustments, the full-scale vanilla method still underperforms relative to the sub-scale version. This performance degradation likely stems from the shallow design of our backbone compared to the heavy architectures utilized in (Edstedt et al., 2024a). Furthermore, while the deformable-based SDDH outperforms vanilla baselines, it fails to match our method in precision and inference speed. Notably, even with kernel fusion acceleration, the full-scale SDDH remains substantially less efficient than our framework. These results confirm the superior effectiveness and efficiency of CLIDD for high-quality local feature representation.

Table 8: **Comparison with dense description architectures.** The experimental results evaluate our sparse extraction strategy against several dense fusion description method.

Model	Description Architecture	FPS	MegaDepth-1500			ScanNet-1500		
			AUC@5°	AUC@10°	AUC@20°	AUC@5°	AUC@10°	AUC@20°
A48	Sub-Scale Vanilla (Yao et al., 2025)	845.3	25.28	36.39	47.46	9.18	18.89	30.77
	Full-Scale Vanilla (Edstedt et al., 2024a)	420.2	13.47	21.15	30.53	5.12	12.06	21.90
	Full-Scale SDDH (Zhao et al., 2023)	162.4	42.56	54.27	63.93	11.42	23.39	36.66
	Ours	881.1	<b>44.98</b>	<b>57.13</b>	<b>66.41</b>	<b>12.62</b>	<b>25.35</b>	<b>39.23</b>
U128	Sub-Scale Vanilla (Yao et al., 2025)	170.2	60.82	73.07	81.94	18.28	35.00	51.09
	Full-Scale Vanilla (Edstedt et al., 2024a)	164.6	56.16	67.89	76.65	17.33	33.91	49.87
	Full-Scale SDDH (Zhao et al., 2023)	64.6	63.28	75.63	84.51	17.93	33.91	51.45
	Ours	281.4	<b>64.75</b>	<b>77.15</b>	<b>85.77</b>	<b>18.94</b>	<b>36.46</b>	<b>53.66</b>

Table 9: **Ablation of descriptor loss weighting.** Performance comparison across different weight balances for the DualSoftmax loss and the Orthogonal-Procrustes loss.

Model	$w_{DS}$	$w_{OP}$	MegaDepth-1500			ScanNet-1500		
			AUC@5°	AUC@10°	AUC@20°	AUC@5°	AUC@10°	AUC@20°
A48	0	1	43.98	55.93	65.17	11.86	23.91	37.09
	0.05	1	<b>44.98</b>	<b>57.13</b>	<b>66.41</b>	<b>12.62</b>	<b>25.35</b>	<b>39.23</b>
	0.1	1	42.30	54.93	65.25	11.16	23.37	37.56
	1	0	33.87	46.65	57.99	9.86	21.12	34.05
N64	0	1	52.71	64.21	72.80	13.97	27.83	42.01
	0.05	1	52.51	64.40	73.11	14.13	27.82	42.21
	0.1	1	<b>53.91</b>	<b>65.81</b>	<b>75.12</b>	<b>14.88</b>	<b>29.34</b>	<b>44.35</b>
	0.5	1	53.62	65.53	74.31	14.50	29.14	44.24
T64	1	0	50.49	62.87	71.98	14.93	29.25	44.27
	0	1	53.55	65.73	74.54	14.86	28.64	43.00
	0.1	1	<b>55.54</b>	<b>67.47</b>	76.27	15.24	29.36	44.06
	0.5	1	54.26	66.74	76.16	15.33	<b>31.03</b>	<b>47.37</b>
	1	1	54.53	67.15	<b>76.32</b>	<b>15.63</b>	30.65	46.18
	1	0	53.94	66.44	75.57	15.49	30.72	46.27

### 5.5.3 Descriptor Loss Analysis

We examine the influence of descriptor loss components by testing various weight combinations of the DualSoftmax loss  $L_{DS}$  for direct supervision and the Orthogonal-Procrustes loss  $L_{OP}$  for description distillation. This experiment targets lightweight architectures to determine how different supervision strategies affect feature discriminability under capacity constraints. By evaluating configurations ranging from pure distillation to pure direct training, we identify the optimal weighting required to achieve high accuracy in small-scale models.

The results in Table 9 indicate that the distillation loss is vital for the most lightweight architectures. For the minimalist A48 variant, the highest accuracy is achieved when the direct supervision weight  $w_{DS}$  is reduced to 0.05. Relying solely on the direct metric loss leads to a significant performance drop for this architecture. As model capacity grows, the optimal weight for direct supervision gradually increases. For instance, the N64 and T64 models reach peak performance with  $w_{DS}$  values of 0.1 and 0.5, respectively. However, the performance improvements from distillation for the T64 model are relatively limited compared to those observed for the A48 and N64 variants. This trend sug-

gests that higher-capacity models can effectively leverage ground-truth signals with less reliance on external teacher guidance. Nevertheless, a balanced combination of both losses consistently outperforms single-loss strategies across all tested scales. These findings confirm that mixed supervision is critical for maximizing the potential of lightweight descriptor models.

### 5.5.4 Efficiency of Kernel Fusion

We evaluate the impact of kernel fusion on inference efficiency across all model variants using various keypoint counts. Throughput is measured for each architecture while processing between 1,024 and 16,384 keypoints. As illustrated in Fig. 6, where both axes use a  $\log_2$  scale, the fused kernel implementation consistently delivers significantly higher throughput than the non-fused baseline. This efficiency gap widens as the model scale and the number of keypoints increase, demonstrating the superior scalability of our hardware-aware design.

The scaling behavior highlights the distinct advantages of our approach. Without kernel fusion, the FPS halves almost immediately as the number of sampling points doubles. This indicates that the system is bound

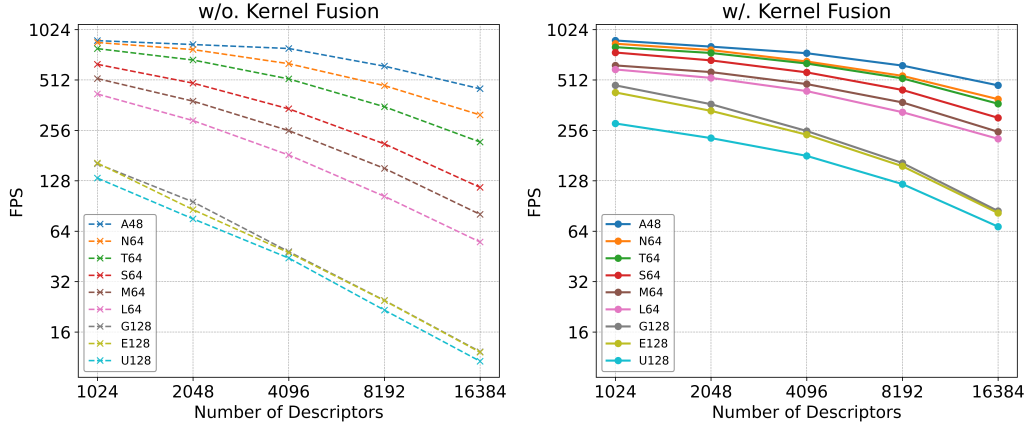


Fig. 6: **Throughput comparison across various model scales and keypoint counts.** The results visualize the inference efficiency with (solid) and without (dashed) kernel fusion. Both the number of sampling points and the FPS results are presented on a  $\log_2$  scale.

Table 10: **Evaluation of descriptor discriminativeness under varying spatial densities.** Comparison of matching performance across different keypoint limits and NMS configurations for multiple model scales.

Method	Config		MegaDepth-1500			ScanNet-1500			IMC2022	
	Max N	NMS	AUC@5°	AUC@10°	AUC@20°	AUC@5°	AUC@10°	AUC@20°	Private	Public
A48	4k	✓	44.98	57.13	66.41	12.62	25.35	39.23	0.473	0.492
	4k	✗	48.84	61.06	70.32	14.45	28.03	42.31	0.493	0.511
	10k	✗	<b>51.96</b>	<b>63.65</b>	<b>72.26</b>	<b>15.37</b>	<b>29.86</b>	<b>44.31</b>	<b>0.530</b>	<b>0.548</b>
N64	4k	✓	53.91	65.81	75.12	14.88	29.34	44.35	0.583	0.588
	4k	✗	56.62	68.69	77.24	16.33	31.63	46.87	0.601	0.612
	10k	✗	<b>58.43</b>	<b>70.46</b>	<b>79.08</b>	<b>17.30</b>	<b>32.99</b>	<b>48.09</b>	<b>0.636</b>	<b>0.644</b>
T64	4k	✓	54.26	66.74	76.16	15.33	31.03	47.37	0.577	0.597
	4k	✗	57.01	69.43	78.56	17.05	33.07	48.92	0.604	0.613
	10k	✗	<b>59.17</b>	<b>71.53</b>	<b>80.23</b>	<b>17.70</b>	<b>33.83</b>	<b>49.79</b>	<b>0.624</b>	<b>0.641</b>
S64	4k	✓	55.43	67.74	77.28	16.74	31.96	47.77	0.603	0.605
	4k	✗	57.16	70.34	80.04	17.90	33.72	48.75	0.616	0.620
	10k	✗	<b>59.73</b>	<b>72.48</b>	<b>81.63</b>	<b>18.66</b>	<b>34.84</b>	<b>50.00</b>	<b>0.642</b>	<b>0.653</b>
M64	4k	✓	57.41	69.81	78.62	17.28	33.55	49.36	0.602	0.605
	4k	✗	58.99	71.70	80.77	18.13	34.66	50.48	0.637	0.633
	10k	✗	<b>61.55</b>	<b>73.84</b>	<b>82.67</b>	<b>19.02</b>	<b>35.45</b>	<b>51.01</b>	<b>0.666</b>	<b>0.665</b>
L64	4k	✓	58.29	70.83	80.02	17.86	33.59	49.33	0.619	0.617
	4k	✗	59.72	72.22	81.38	<b>18.54</b>	<b>34.77</b>	50.50	0.644	0.649
	10k	✗	<b>62.06</b>	<b>74.47</b>	<b>83.03</b>	18.52	34.60	<b>50.56</b>	<b>0.678</b>	<b>0.681</b>
G128	4k	✓	62.22	74.61	83.08	18.52	35.04	51.85	0.689	0.686
	4k	✗	62.94	75.33	84.08	18.88	35.99	52.52	0.694	0.692
	10k	✗	<b>64.85</b>	<b>77.11</b>	<b>85.54</b>	<b>19.47</b>	<b>36.59</b>	<b>52.74</b>	<b>0.704</b>	<b>0.708</b>
E128	4k	✓	62.84	75.16	83.72	18.35	35.38	51.97	0.695	0.694
	4k	✗	64.07	76.45	84.76	<b>19.49</b>	<b>36.61</b>	<b>53.25</b>	0.700	0.697
	10k	✗	<b>65.38</b>	<b>77.56</b>	<b>85.87</b>	18.63	35.89	52.63	<b>0.713</b>	<b>0.714</b>
U128	4k	✓	64.75	77.15	85.77	<b>18.94</b>	36.46	53.66	0.717	0.716
	10k	✗	<b>67.40</b>	<b>79.21</b>	<b>87.25</b>	18.58	<b>36.50</b>	53.56	<b>0.729</b>	<b>0.732</b>

by the high overhead of intermediate tensor management. In contrast, our fused strategy maintains stable performance across a much broader range of sampling densities. For larger configurations, a notable performance drop-off only occurs when the number of keypoints exceeds 10,000. This confirms that kernel fusion effectively minimizes memory bottlenecks and ensures real-time performance even under high-density conditions.

### 5.5.5 Descriptor Discriminativeness Across Varying Spatial Densities

We investigate the discriminative power of our descriptors across varying spatial densities by adjusting keypoint sampling constraints. While our baseline setup uses 4,096 keypoints with NMS to ensure spatial distribution, we further evaluate performance by removing NMS and increasing the sampling limit to 10,000. This procedure verifies whether the descriptors main-

tain high matching accuracy as the feature environment becomes significantly more crowded.

As shown in Table 10, removing NMS and increasing the sampling limit leads to consistent performance gains across all evaluated models. These improvements are particularly significant for smaller models. Our descriptors demonstrate strong discriminative power by resolving matches effectively even as point density increases. Specifically, the configuration with 10,000 points and no NMS yields the highest accuracy on the MegaDepth-1500 and IMC2022 benchmarks.

While removing the NMS stage further enhances post-processing efficiency, its omission can lead to localized clustering in high-texture areas. Spatially uniform points are generally preferred in 3D reconstruction tasks because they provide more robust geometric constraints across the entire scene. Consequently, the decision to employ NMS should be determined by the specific requirements of the target task. This allows users to achieve the optimal balance between matching precision and spatial coverage.

## 6 Conclusions

In this work, we presented a systematic framework for efficient and high-precision local feature representation based on Cross-Layer Independent Deformable Description. By decoupling sampling positions across different feature scales and utilizing kernel fusion, our method successfully extracts unique and diverse local descriptors while maintaining a minimal memory footprint. We demonstrated that our scalable architecture family, trained through a unified distillation and metric learning scheme, provides a versatile range of solutions for various deployment scenarios. Experimental results across multiple geometric benchmarks establish that our method achieves a dual state-of-the-art status, outperforming existing frameworks in both precision and inference throughput. This work confirms that high structural fidelity and discriminative power can be achieved without the heavy computational burden of high-resolution feature maps or dense fusion modules.

While our framework achieves significant improvements in representational quality, keypoints can still exhibit spatial clustering in dense, NMS-free scenarios. This redundancy can limit the overall spatial coverage across the scene. Future research will explore detection mechanisms to promote a more uniform keypoint distribution while maintaining strict inference efficiency.

## Data Availability

All the data used in this paper come from open-source datasets that are freely available for anyone to download. The demo and weights of our work are available at <https://github.com/HITCSC/CLIDD>.

## References

- Agarwal S, Snavely N, Seitz SM, Szeliski R (2010) Bundle adjustment in the large. In: Computer Vision–ECCV 2010: 11th European Conference on Computer Vision, Heraklion, Crete, Greece, September 5–11, 2010, Proceedings, Part II 11, Springer, pp 29–42
- Balntas V, Lenc K, Vedaldi A, Mikolajczyk K (2017) Hpatches: A benchmark and evaluation of hand-crafted and learned local descriptors. In: Proceedings of the IEEE conference on computer vision and pattern recognition, pp 5173–5182
- Barath D, Noskova J, Ivashechkin M, Matas J (2020) Magsac++, a fast, reliable and accurate robust estimator. In: Proceedings of the IEEE/CVF conference on computer vision and pattern recognition, pp 1304–1312
- Dai A, Chang AX, Savva M, Halber M, Funkhouser T, Nießner M (2017a) Scannet: Richly-annotated 3d reconstructions of indoor scenes. In: Proceedings of the IEEE conference on computer vision and pattern recognition, pp 5828–5839
- Dai J, Qi H, Xiong Y, Li Y, Zhang G, Hu H, Wei Y (2017b) Deformable convolutional networks. In: Proceedings of the IEEE international conference on computer vision, pp 764–773
- DeTone D, Malisiewicz T, Rabinovich A (2018) Superpoint: Self-supervised interest point detection and description. In: Proceedings of the IEEE conference on computer vision and pattern recognition workshops, pp 224–236
- Dusmanu M, Rocco I, Pajdla T, Pollefeys M, Sivic J, Torii A, Sattler T (2019) D2-net: A trainable cnn for joint detection and description of local features. arXiv preprint arXiv:190503561
- Edstedt J, Bökman G, Wadenbäck M, Felsberg M (2024a) DeDoDe: Detect, Don’t Describe — Describe, Don’t Detect for Local Feature Matching. In: 2024 International Conference on 3D Vision (3DV), IEEE
- Edstedt J, Bökman G, Zhao Z (2024b) DeDoDe v2: Analyzing and Improving the DeDoDe Keypoint Detector. In: IEEE/CVF Computer Society Conference on Computer Vision and Pattern Recognition Workshops (CVPRW)

Gleize P, Wang W, Feiszli M (2023) Silk: Simple learned keypoints. In: Proceedings of the IEEE/CVF international conference on computer vision, pp 22499–22508

He K, Zhang X, Ren S, Sun J (2016) Deep residual learning for image recognition. In: Proceedings of the IEEE conference on computer vision and pattern recognition, pp 770–778

Howard A, Trulls E, etru1927, Yi KM, old ufo, Dane S, Jin Y (2022) Image matching challenge 2022. URL <https://kaggle.com/competitions/image-matching-challenge-2022>

Katragadda S, Lee W, Peng Y, Geneva P, Chen C, Guo C, Li M, Huang G (2024) Nerf-vins: A real-time neural radiance field map-based visual-inertial navigation system. In: 2024 IEEE International Conference on Robotics and Automation (ICRA), IEEE, pp 10230–10237

Kerbl B, Kopanas G, Leimkühler T, Drettakis G (2023) 3d gaussian splatting for real-time radiance field rendering. *ACM Trans Graph* 42(4):139–1

Larsson V, contributors (2020) PoseLib - Minimal Solvers for Camera Pose Estimation. URL <https://github.com/vlarsson/PoseLib>

Lei X, Wang M, Zhou W, Li H (2025) Gaussnav: Gaussian splatting for visual navigation. *IEEE Transactions on Pattern Analysis and Machine Intelligence*

Leroy V, Cabon Y, Revaud J (2024) Grounding image matching in 3d with mast3r. In: European Conference on Computer Vision, Springer, pp 71–91

Li Z, Snavely N (2018) Megadepth: Learning single-view depth prediction from internet photos. In: Proceedings of the IEEE conference on computer vision and pattern recognition, pp 2041–2050

Loshchilov I (2017) Decoupled weight decay regularization. arXiv preprint arXiv:171105101

Lowe DG (2004) Distinctive image features from scale-invariant keypoints. *International journal of computer vision* 60:91–110

Luo Z, Zhou L, Bai X, Chen H, Zhang J, Yao Y, Li S, Fang T, Quan L (2020) Aslfeat: Learning local features of accurate shape and localization. In: Proceedings of the IEEE/CVF conference on computer vision and pattern recognition, pp 6589–6598

Mildenhall B, Srinivasan PP, Tancik M, Barron JT, Ramamoorthi R, Ng R (2021) Nerf: Representing scenes as neural radiance fields for view synthesis. *Communications of the ACM* 65(1):99–106

Oquab M, Darct T, Moutakanni T, Vo H, Szafraniec M, Khalidov V, Fernandez P, Haziza D, Massa F, El-Nouby A, et al. (2023) Dinov2: Learning robust visual features without supervision. arXiv preprint arXiv:230407193

Potje G, Cadar F, Araujo A, Martins R, Nascimento ER (2024) Xfeat: Accelerated features for lightweight image matching. In: Proceedings of the IEEE/CVF Conference on Computer Vision and Pattern Recognition, pp 2682–2691

Radenović F, Iscen A, Tolias G, Avrithis Y, Chum O (2018) Revisiting oxford and paris: Large-scale image retrieval benchmarking. In: Proceedings of the IEEE/CVF Conference on Computer Vision and Pattern Recognition, pp 5706–5715, DOI 10.1109/CVPR.2018.00598

Rublee E, Rabaud V, Konolige K, Bradski G (2011) Orb: An efficient alternative to sift or surf. In: 2011 International conference on computer vision, Ieee, pp 2564–2571

Sarlin PE, Cadena C, Siegwart R, Dymczyk M (2019) From coarse to fine: Robust hierarchical localization at large scale. In: CVPR

Sattler T, Maddern W, Toft C, Torii A, Hammarstrand L, Stenborg E, Safari D, Okutomi M, Pollefeys M, Sivic J, et al. (2018) Benchmarking 6dof outdoor visual localization in changing conditions. In: Proceedings of the IEEE conference on computer vision and pattern recognition, pp 8601–8610

Schönemann PH (1966) A generalized solution of the orthogonal procrustes problem. *Psychometrika* 31(1):1–10

Sun J, Shen Z, Wang Y, Bao H, Zhou X (2021) Loftr: Detector-free local feature matching with transformers. In: Proceedings of the IEEE/CVF conference on computer vision and pattern recognition, pp 8922–8931

Taira H, Okutomi M, Sattler T, Cimpoi M, Pollefeys M, Sivic J, Pajdla T, Torii A (2018) Inloc: Indoor visual localization with dense matching and view synthesis. In: Proceedings of the IEEE Conference on Computer Vision and Pattern Recognition, pp 7199–7209

Tang J, Kim H, Guizilini V, Pillai S, Ambrus R (2019) Neural outlier rejection for self-supervised keypoint learning. arXiv preprint arXiv:191210615

Tyszkiewicz M, Fua P, Trulls E (2020) Disk: Learning local features with policy gradient. *Advances in Neural Information Processing Systems* 33:14254–14265

Wang C, Xu R, Lu K, Xu S, Meng W, Zhang Y, Fan B, Zhang X (2023) Attention weighted local descriptors. *IEEE Transactions on Pattern Analysis and Machine Intelligence* 45(9):10632–10649

Wang J, Chen M, Karaev N, Vedaldi A, Rupprecht C, Novotny D (2025) Vggt: Visual geometry grounded transformer. In: Proceedings of the Computer Vision and Pattern Recognition Conference, pp 5294–5306

Wang S, Leroy V, Cabon Y, Chidlovskii B, Revaud J (2024a) Dust3r: Geometric 3d vision made easy. In:

Proceedings of the IEEE/CVF Conference on Computer Vision and Pattern Recognition, pp 20697–20709

Wang Y, He X, Peng S, Tan D, Zhou X (2024b) Efficient loftr: Semi-dense local feature matching with sparse-like speed. In: Proceedings of the IEEE/CVF Conference on Computer Vision and Pattern Recognition, pp 21666–21675

Xia Z, Pan X, Song S, Li LE, Huang G (2022) Vision transformer with deformable attention. In: Proceedings of the IEEE/CVF conference on computer vision and pattern recognition, pp 4794–4803

Xiong Y, Li Z, Chen Y, Wang F, Zhu X, Luo J, Wang W, Lu T, Li H, Qiao Y, et al. (2024) Efficient deformable convnets: Rethinking dynamic and sparse operator for vision applications. In: Proceedings of the IEEE/CVF conference on computer vision and pattern recognition, pp 5652–5661

Yao H, Hao N, Xie C, He F (2024) Edgepoint: Efficient point detection and compact description via distillation. In: 2024 IEEE International Conference on Robotics and Automation (ICRA), IEEE, pp 766–772

Yao H, He F, Hao N, Xie C (2025) Edgepoint2: Compact descriptors for superior efficiency and accuracy. arXiv preprint arXiv:250417280

Zhao X, Wu X, Miao J, Chen W, Chen PC, Li Z (2022) Alike: Accurate and lightweight keypoint detection and descriptor extraction. IEEE Transactions on Multimedia 25:3101–3112

Zhao X, Wu X, Chen W, Chen PC, Xu Q, Li Z (2023) Aliked: A lighter keypoint and descriptor extraction network via deformable transformation. IEEE Transactions on Instrumentation and Measurement 72:1–16

Zhu X, Hu H, Lin S, Dai J (2019) Deformable convnets v2: More deformable, better results. In: Proceedings of the IEEE/CVF conference on computer vision and pattern recognition, pp 9308–9316